Modulated Model Predictive Current Control With Active Damping for LC-Filtered PMSM Drives

Changming Zheng, *Member, IEEE*, Miao Xie, Xuanxuan Dong, Zheng Gong, *Member, IEEE*, Tomislav Dragičević, *Senior Member, IEEE*, and Jose Rodriguez, *Life Fellow, IEEE*

***Abstract*— LC-filtered permanent magnet synchronous motor (LC-PMSM) system is suitable for long-cable drives but it has inherent resonant stability issues. This article presents a modulated model predictive current controller with active damping (AD-M^{2}PCC) for stabilizing the LC-PMSM drive system. First, to avoid the complex exponentiation operations in typical model predictive current control (MPCC), a simplified reduced-order predictive model is constructed and a baseline MPCC is derived based on inverter-side current reference tracking, reducing the computational burden and enhancing the robustness to the model mismatches. Then, a capacitor-current-feedback active damping (AD) is integrated into MPCC for resonance suppression. It has an intuitive damping concept and only one design parameter, significantly lessening the tuning effort. Further, a low-complexity AD-M^{2}PCC scheme is established, which features simple implementation, improved steady-state performance and effective resonance damping. Comparative experimental results are provided to verify the feasibility of the proposed control scheme.**

***Index Terms*— LC filter, model predictive control (MPC), permanent magnet synchronous motor (PMSM), resonance suppression.**

I. Introduction

PERMANENT magnet synchronous motor (PMSM) drive system has attracted widespread attention in industrial sectors in recent years due to its advantages of small size, high power density, and high reliability [1], [2]. Especially in areas of oilfield drilling and mining fields, PMSMs are often placed far away from the voltage–source inverters (VSIs), and the two are connected by long power cables. During the long cable transmission process, the high dv/dt values of VSIs may lead to issues of reflected overvoltages and electromagnetic interference. This is particularly noteworthy as the use of wide bandgap semiconductor devices (e.g., silicon carbide and gallium nitride) becomes increasingly widespread [3], [4], [5]. In this context, the overlong power cable will cause severe motor overvoltage, bearing damage, and insulation aging problems [6]. An effective solution is to install an LC filter on the output side of the VSI, forming an LC-filtered PMSM (LC-PMSM) drive system [7], [8], [9]. Then, the voltage and current applied to PMSMs are almost the sinusoidal waveforms, which is beneficial for extending the motors' lifespan. Nevertheless, the output LC filter and the stator inductance of PMSM will form a third-order LCL-filter structure, which not only increases the system complexity but also induces resonance issues. Consequently, the operation stability of the LC-PMSM system will be degraded. To this end, exploring a high-performance current control strategy with a simple structure and high stability for the LC-PMSM system is a key issue to be solved.

Various approaches for solving the resonance issues of the LC-PMSM system have been proposed. In [10] and [11], a cascaded proportional-integral (PI) control scheme is proposed to handle the resonance induced by the LC filter. However, multiple design parameters are introduced in this control method, and the tuning effort is large and hard to adapt to various working conditions. In addition, the dynamic response of the system deteriorates due to the bandwidth limitations of outer control loops [12]. To simplify the control implementation, a passive damping method is proposed by adding a physical resistor in parallel or series with the LC filter, but it may increase the power loss [13]. To avoid affecting the system's efficiency, the active-damping (AD) method provides a good alternative solution. In [14], an AD method with capacitor-voltage feedback is proposed to suppress the resonance of the induction motor with an LC filter by serially connecting a virtual resistor to the filter capacitance. Similarly, a virtual resistor is placed in parallel with the capacitor to realize the AD [15], [16]. In [17], a feedforward method is proposed to enhance the stability of the LC-filtered induction motor. It is realized by adding an inverter-voltage feedforward term to the stator current reference. In [18], a variable delay time control technique is proposed to solve the resonance issues without using an extra damping term. Nevertheless, the above control approaches are designed based on the conventional PI control framework, resulting in tedious parameter-tuning work and unsatisfied dynamic response. Moreover, multiple PI parameters are coupled with each other,

Manuscript received 17 February 2024; revised 2 May 2024; accepted 29 May 2024. Date of publication 31 May 2024; date of current version 2 August 2024. This work was supported in part by the National Natural Science Foundation of China under Grant 52107217 and Grant 52277205, and in part by the Natural Science Foundation of Jiangsu Province under Grant BK20230108. Recommended for publication by Associate Editor Debaprasad Kastha. *(Corresponding author: Zheng Gong.)*

Changming Zheng, Miao Xie, Xuanxuan Dong, and Zheng Gong are with the School of Electrical Engineering, China University of Mining and Technology, Xuzhou 221116, China (e-mail: changming@cumt.edu.cn; xiemiao@cumt.edu.cn; ts22230012a31@cumt.edu.cn; zgo@cumt.edu.cn).

Tomislav Dragičević is with the Center of Electric Power and Energy, Technical University of Denmark, 2800 Kongens Lyngby, Denmark (e-mail: tomdr@elektro.dtu.dk).

Jose Rodriguez is with the Faculty of Engineering, Universidad San Sebastian, Santiago 8420524, Chile (e-mail: jose.rodriguezp@uss.cl).

Color versions of one or more figures in this article are available at https://doi.org/10.1109/JESTPE.2024.3408070.

Digital Object Identifier 10.1109/JESTPE.2024.3408070

which means if they are not properly set, the system stability cannot be guaranteed.

Recently, model predictive control (MPC) strategies are considered to be effective solutions for achieving high-performance control of PMSM drives. It has the advantages of simple structure, inherent decoupling capability, and multiple-objective optimization [19], [20], [21], [22]. The fundamental principle of MPC is utilizing the discrete model of the system to evaluate a predesigned cost function. The optimal control input for predicting future states is then obtained and applied to VSI [23], [24], [25]. Generally, MPC can be classified as finite-set MPC and modulated MPC schemes, which have been widely applied to conventional PMSM drives. Typical finite-set MPC applies a single voltage vector during a control period. Since no modulator is employed, it may cause an unsatisfactory steady-state response. Till now, the application of finite-set MPC to LC-filtered motor drives has been preliminarily explored. In [26], a finite-set model predictive current control (MPCC) is proposed for medium-voltage drives with an LC filter. This method mainly focuses on the stator-current-tracking control objective, but the suppression of the system resonance is not considered. In [27], a three-objective finite-set MPCC is proposed, which can mitigate the resonance problem to some degree. However, it has a non-negligible computational burden and multiple weighting factors to be designed. Tuning them to ensure an optimal balance between different control objectives is challenging due to the lack of analytical design. In [28], a long-prediction-horizon MPCC is proposed, enhancing the system's steady-state performance but with a significant computational amount. Nonetheless, the above MPCC methods will inherit the deficiencies of finite-set MPC, such as large steady-state ripples, variable switching frequencies, and wide distributions of harmonic spectrum [29]. These issues may not only hinder the design of the LC filter but also trigger unknown resonance dynamics.

To tackle the weaknesses of finite-set MPC, various modulated/multivector MPC schemes have been proposed. Modulated MPC methods perform multiple voltage vectors with optimally calculated duty cycles over a control period, which can improve steady-state performance. In [30], a dual-vector modulated MPC scheme is proposed for induction motor drives. Two voltage vectors with optimal duty cycles are applied per control period, reducing the output current ripples. Similarly, two dual-vector MPC schemes with different duty-cycle calculation ways are presented and compared in [31]. Although dual-vector MPC can enhance steady-state performance compared to finite-set MPC, the amplitude and angle of the synthesized vector are limited and the control degree of freedom is not maximized, making it difficult to achieve optimal performance. In this context, the three-vector modulated MPC scheme is proposed and widely applied in PMSM drives [32], [33]. This method performs three voltage vectors during a control period, thus achieving optimal steady-state performance and a fixed switching frequency. In [34], a three-vector MPCC is proposed, which is realized by introducing virtual vectors to expand the vector control set. Its steady-state performance is improved, while the computational burden is also increased. In [35], a low-complexity three-vector MPC is proposed for PMSM drives based on an offline table. In [36] and [37], a modified three-vector MPC considering the overmodulation is proposed. By optimizing the duty-cycle time, the over-modulation capability is enhanced and the current harmonics are reduced. Nonetheless, the modulated MPC schemes above are designed solely for stator-current control of first-order PMSM systems. To the best of our knowledge, no reference has reported this control strategy for third-order LC-PMSM drives. One reason is that the adoption of an LC filter makes it difficult to calculate the duty cycle. Moreover, the resonances arising from the LC-PMSM system cannot be directly handled by the existing stator-current-based MPC framework. As a result, direct implementation of existing modulated MPC to LC-PMSM becomes challenging, and exploring a modulated MPC framework that is simple to implement and easy to integrate resonance damping is of both practical and scientific interest.

To this end, this article presents an AD-based modulated MPCC scheme for stabilizing the LC-PMSM system. The main contributions are summarized below.

1) A simplified reduced-order predictive model is established and the inverter-side current tracking-based baseline MPCC is derived, which can reduce the control order and computational burden compared to typical MPCC.
2) A capacitor-current-feedback AD technique is further integrated into the baseline MPCC, which can provide an intuitive AD concept, sufficient resonance suppression, and reduced tuning effort compared to typical MPCC.
3) A modulated AD-MPCC (AD-M^{2}PCC) framework suitable for the LC-PMSM system is proposed, featuring low complexity, satisfactory steady-state performance, and strong robustness to parameter mismatches. Moreover, this framework has strong universality, making it possible to extend existing multivector MPCC to the LC-PMSM system.

The remainder of this article is arranged below. Section II introduces the description of the LC-PMSM drives, including system modeling and the effects of the LC filter. The basics of a typical MPCC scheme are introduced in Section III. Section IV elaborates on the principle of the proposed AD-M^{2}PCC scheme. Section V presents the parameter design criteria. Section VI gives the experimental results, and the conclusion is summarized in Section VII.

II. Description of LC-PMSM System

A. System Configuration and Modeling

The basic configuration of a VSI-fed LC-PMSM drive system is depicted in Fig. 1, where a two-level three-phase VSI with an output LC filter is connected with a surface-mounted PMSM. In Fig. 1, $V_{\rm dc}$ is the dc-link voltage. S_1 to S_6 are bridge-arm switches of VSI. L_f and C_f are filter inductance and capacitance. v_i, i_f, v_s, and i_s denote the inverter voltage, inverter-side current, per-phase filter capacitor voltage, and stator current, respectively. ω_m is mechanical angular velocity of PMSM.

Accordingly, the continuous-time state-space model of the LC-PMSM system in dq-axis rotating coordinate frame is

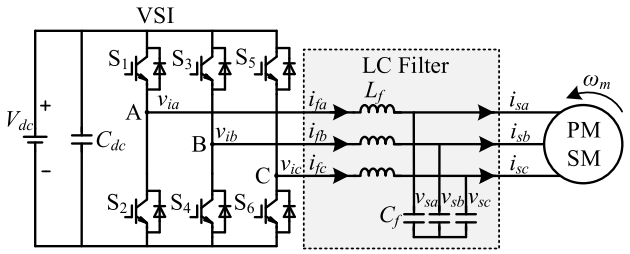

Fig. 1. Basic configuration of a VSI-fed LC-PMSM drive system.

established as follows:

$$\dot{\mathbf{x}} = \mathbf{A}\mathbf{x} + \mathbf{B}\mathbf{v}_i + \mathbf{D} \tag{1}$$

where the system state variable matrix $\mathbf{x} = [\,i_{fd}\;\; i_{fq}\;\; v_{sd}\;\; v_{sq}\;\; i_{sd}\;\; i_{sq}\,]^T$, the inverter voltage or system control input matrix $\mathbf{v}_i = [v_{id}\;\; v_{iq}]^T$, and the system matrices are described as

$$\mathbf{A} = \begin{bmatrix} 0 & \omega_e & -\frac{1}{L_f} & 0 & 0 & 0 \\ -\omega_e & 0 & 0 & -\frac{1}{L_f} & 0 & 0 \\ \frac{1}{C_f} & 0 & 0 & \omega_e & -\frac{1}{C_f} & 0 \\ 0 & \frac{1}{C_f} & -\omega_e & 0 & 0 & -\frac{1}{C_f} \\ 0 & 0 & \frac{1}{L_s} & 0 & -\frac{R_s}{L_s} & \omega_e \\ 0 & 0 & 0 & \frac{1}{L_s} & -\omega_e & -\frac{R_s}{L_s} \end{bmatrix}$$

$$\mathbf{B} = \begin{bmatrix} \frac{1}{L_f} & 0 \\ 0 & \frac{1}{L_f} \\ 0 & 0 \\ 0 & 0 \\ 0 & 0 \\ 0 & 0 \end{bmatrix}, \quad \mathbf{D} = \begin{bmatrix} 0 & 0 & 0 & 0 & 0 & -\frac{\omega_e \psi_f}{L_s} \end{bmatrix}^T.$$

R_s, L_s, and ψ_f are stator resistance, stator inductance, and rotor flux. ω_e is electromagnetic angular velocity of surfaced-mounted PMSM.

B. Effects of LC Filter on PMSM Drives

The LC-PMSM system has some differences compared to the typical PMSM system without an LC filter. The effects of the LC filter on PMSM drives have been investigated in [8], [10], and [9], which confirms that the LC-PMSM system has better efficiency, lower voltage stress, and leakage current. Here, we analyze the impacts of the LC filter on PMSM drives from the viewpoint of the frequency domain.

For typical PMSM drives without LC filter, the system open-loop transfer function in dq-axis complex form can be expressed as

$$G_L(s) = \frac{\mathbf{i}_{sdq}(s)}{\mathbf{v}_{idq}(s)} = \frac{1}{L_s s + R_s} \tag{2}$$

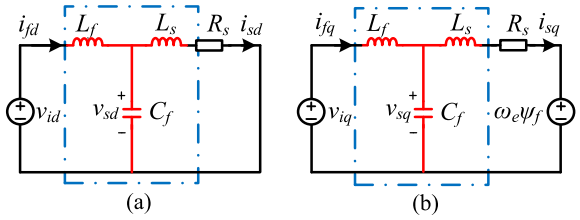

Fig. 2. dq-axis equivalent circuit of the LC-PMSM system. (a) d-axis. (b) q-axis.

TABLE I
NOMINAL PARAMETERS OF AN LC-PMSM SYSTEM

Constants	Symbols	Values
Rated Power	P_N	300 W
DC-link voltage	V_{dc}	150 V
Filter inductance	L_f	2 mH
Filter capacitance	C_f	10 μF
Stator inductance	L_s	2.35 mH
Stator resistance	R_s	0.4 Ω
Rotor flux linkage	ψ_f	0.153 Wb
Number of pole pairs	p	4
Rated rotor speed	n_0, f_0	1000 rpm, 66.67 Hz

where the state variables with subscript dq denote the complex vector, i.e., $\mathbf{x}_{dq} = x_d + jx_q$.

In contrast, for the LC-PMSM system, neglecting the dq-axis cross-coupling term, the dq-axis equivalent circuit of the system can be obtained, which is shown in Fig. 2. It can be seen that an LCL-filter structure is formed by the LC filter and the stator inductance. Correspondingly, the open-loop transfer function of the LC-PMSM system can be derived as

$$\begin{aligned} G_{LC}(s) &= \frac{\mathbf{i}_{sdq}(s)}{\mathbf{v}_{idq}(s)} \\ &= \frac{1}{C_f L_f L_s s^3 + C_f L_f R_s s^2 + (L_f + L_s)s + R_s}. \end{aligned} \tag{3}$$

By comparing (2) and (3), it is easy to deduce that the LC-PMSM becomes a third-order system compared to the typical first-order PMSM system. Moreover, the bode plots of $G_L(s)$ and $G_{LC}(s)$ are depicted in Fig. 3 using the parameters listed in Table I. As is shown, the adoption of an LC filter will somewhat degrade the dynamic performance of typical PMSM drives. When different filter inductance is used, the 0-dB gain crossover frequency of $G_{LC}(s)$ will be decreased with the increase of L_f, while the phase margin does not change so much. Hence, the dynamic response of LC-PMSM will be slower than that of a typical PMSM system. Meanwhile, deploying different filter capacitance C_f does not affect the low and mediate frequency characteristics of LC-PMSM. Moreover, it can be observed that the LC-PMSM system has better high-frequency harmonic attenuation but may induce a resonance peak under certain LC-filter parameters, which will cause the system's instability. The resulting resonant frequency

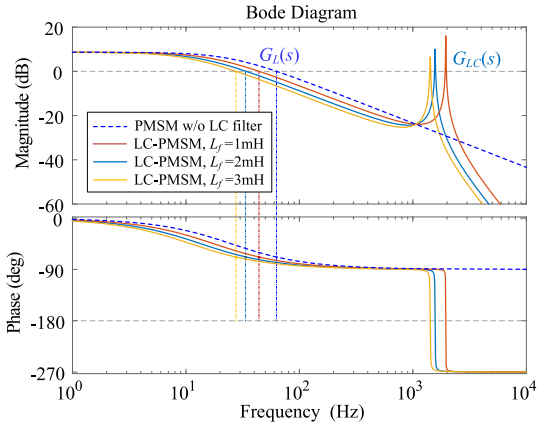

(a)

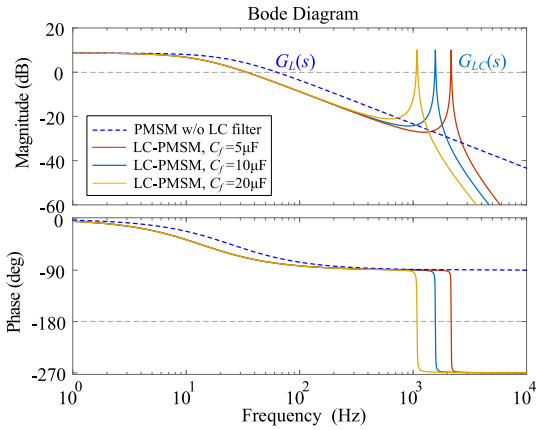

(b)

Fig. 3. Bode plots of $G_L(s)$ (PMSM w/o LC filter) and $G_{LC}(s)$ under different LC-filter parameters. (a) $L_f = 1$, 2, and 3 mH, $C_f = 10$ μF. (b) $C_f = 5$, 10, and 20 μF, $L_f = 2$ mH.

of the system can be calculated as follows:

$$f_{\text{res}} = \frac{1}{2\pi}\sqrt{\frac{L_f + L_s}{C_f L_f L_s}}. \tag{4}$$

Therefore, it is urgent to design a high-performance current controller, enabling simple implementation and sufficient resonance-suppression capability.

III. Basics of Typical MPCC for LC-PMSM

The fundamental control framework for the LC-PMSM system is stator-current tracking vector control. The outer control loop is usually a speed controller, which provides the reference for the inner-loop q-axis stator current. Meanwhile, the d-axis stator current is controlled to be 0 for surface-mounted PMSM. Till now, the state-of-the-art MPCC is a three-objective MPCC scheme proposed in [27]. It has three control objectives including stator-current, capacitor-voltage, and inductor-current reference tracking, which is designed based on a finite control set, as given below.

A. Three-Objective Cost Function

As explained in [27], the stator current, capacitor voltage, and inductor current are simultaneously controlled to suppress the resonance. As a result, a three-objective cost function is designed as follows:

$$\begin{aligned} g_{\text{con}} &= g_1 + w_v g_2 + w_i g_3 \\ &= \left[\mathbf{x}_{k+1} - \mathbf{x}^*\right]^T \mathbf{W} \left[\mathbf{x}_{k+1} - \mathbf{x}^*\right] \end{aligned} \tag{5}$$

where the three control objectives g_1, g_2, and g_3 are

$$\begin{cases} g_1 = (i_{sd}^* - i_{sd,k+1})^2 + (i_{sq}^* - i_{sq,k+1})^2 \\ g_2 = (v_{sd}^* - v_{sd,k+1})^2 + (v_{sq}^* - v_{sq,k+1})^2 \\ g_3 = (i_{fd}^* - i_{fd,k+1})^2 + (i_{fq}^* - i_{fq,k+1})^2. \end{cases}$$

The state reference vector $\mathbf{x}^* = [i_{fd}^* \;\; i_{fq}^* \;\; v_{sd}^* \;\; v_{sq}^* \;\; i_{sd}^* \;\; i_{sq}^*]^T$. The weighting factor matrix $\mathbf{W} = \text{diag}(w_i, w_i, w_v, w_v, 1, 1)$.

B. Full-Order Predictive Model

Since all the six state variables are controlled in the cost function g_{con}, the full-order discrete predictive model should be constructed based on system model (1). To establish the relationships between six predictive values and control input, the third-order Taylor series expansion approximation is employed to compute the discrete system matrices as

$$\mathbf{A}_{d,6\times 6} \approx \sum_{i=0}^{3} \frac{\mathbf{A}^i T_s^i}{i!} \tag{6}$$

$$\mathbf{B}_{d,6\times 2} \approx \sum_{i=1}^{3} \frac{\mathbf{A}^{i-1} T_s^i}{i!}\mathbf{B}, \quad \mathbf{D}_{d,6\times 1} \approx \sum_{i=1}^{3} \frac{\mathbf{A}^{i-1} T_s^i}{i!}\mathbf{D} \tag{7}$$

where T_s is the sampling period.

Then, the full-order predictive model of typical MPCC can be derived based on (6) and (7) as

$$\mathbf{x}_{k+1} = \mathbf{A}_d \mathbf{x}_k + \mathbf{B}_d \mathbf{v}_{i,k} + \mathbf{D}_d \tag{8}$$

where subscript k and $k+1$ represent kT_s and $(k+1)T_s$ time instant.

C. Computation Delay Compensation

In actual digital implementations, since the controller requires time to sample and execute the algorithm, the optimal control vector would be acted at the next T_s, resulting in a one-step computation delay [22], [27]. This inherent delay will deteriorate the steady-state performance or even cause system instability. To compensate for this delay, a commonly used method is one-step forward prediction or observation, which is realized by using the $(k+2)$th step values in the predictive model, i.e.,

$$\mathbf{x}_{k+2} = \mathbf{A}_d \mathbf{x}_{k+1} + \mathbf{B}_d \mathbf{v}_{i,k+1} + \mathbf{D}_d \tag{9}$$

where $\mathbf{x}_{k+1}$ is calculated by applying the optimal control vector at the previous time step. $\mathbf{v}_{i,k+1}$ is the dq-axis candidate voltage vectors to be evaluated, which are obtained from Table II by the following Park transformation:

$$\mathbf{v}_{i,k+1} = \mathbf{C}_{\text{park}} \mathbf{v}_{\alpha\beta,i} \tag{10}$$

where $\mathbf{C}_{\text{park}} = \begin{bmatrix} \cos\theta & \sin\theta \\ -\sin\theta & \cos\theta \end{bmatrix}$ is the Park transformation matrix. θ is the rotor electrical angle of PMSM. $\mathbf{v}_{\alpha\beta,i} = [v_{\alpha,i} \quad v_{\beta,i}]^T$ with $v_{\alpha,i}$ and $v_{\beta,i}$ being $\alpha\beta$-axis component of candidate voltage vectors in Table II.

TABLE II
CANDIDATE VOLTAGE VECTORS AND SWITCHING STATES OF A VSI

i	Switching states S_i			Basic voltage vector $\mathbf{v}_{\alpha\beta,i}$	
	S_1	S_3	S_5	$v_{\alpha,i}$	$v_{\beta,i}$
0	[0	0	0]	0	0
1	[1	0	0]	$2V_{dc}/3$	0
2	[1	1	0]	$V_{dc}/3$	$\sqrt{3}V_{dc}/3$
3	[0	1	0]	$-V_{dc}/3$	$\sqrt{3}V_{dc}/3$
4	[0	1	1]	$-2V_{dc}/3$	0
5	[0	0	1]	$-V_{dc}/3$	$-\sqrt{3}V_{dc}/3$
6	[1	0	1]	$V_{dc}/3$	$-\sqrt{3}V_{dc}/3$
7	[1	1	1]	0	0

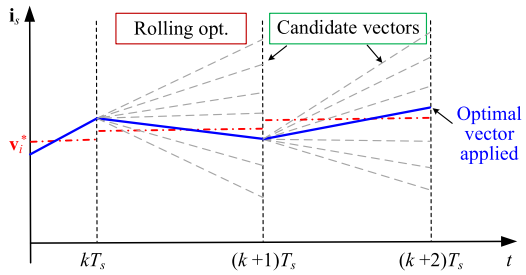

Fig. 4. Rolling optimization principle of typical MPCC.

D. Optimal Vector Selection and Implementation

Replacing $\mathbf{x}_{k+1}$ in (5) with $\mathbf{x}_{k+2}$ in (9), the cost function g_{con} can be evaluated online by enumerating eight candidate voltage vectors of VSI. To reduce the computational burden in digital implementations, the cost function (5) can be simplified using the optimal voltage-reference tracking

$$g_{\text{con}} = \left[\mathbf{v}_{i,k+1} - \mathbf{v}_i^*\right]^T \left[\mathbf{v}_{i,k+1} - \mathbf{v}_i^*\right] \tag{11}$$

where $\mathbf{v}_i^*$ is obtained by setting the gradient of (5) concerning $\mathbf{v}_{i,k}$ to zero as

$$\mathbf{v}_i^* = \left(\mathbf{B}_d{}^T \mathbf{W} \mathbf{B}_d\right)^{-1} \mathbf{B}_d{}^T \mathbf{W} \left[\mathbf{x}^* - \mathbf{A}_d \mathbf{x}_{k+1} - \mathbf{D}_d\right]. \tag{12}$$

The rolling-optimization principle of typical MPCC is depicted in Fig. 4. By enumerating eight candidate voltage vectors of the VSI, the optimal voltage vector that can minimize (11) is selected and the corresponding six optimal switching states are directly applied to the VSI.

It should be mentioned that typical MPCC employs a six-order predictive model with third-order Taylor series expansion approximation, the matrix operations from (6)–(12) will lead to a considerable computational burden and high sensitivity to model parameter mismatches. Moreover, although this method includes three control objectives, it is essentially a finite-set MPC, which leads to unsatisfactory steady-state performance and unfixed switching frequency. The aforementioned shortcomings cannot ensure high control accuracy and are not friendly to the LC filter's design, somewhat hindering the engineering applications of typical MPCC.

IV. PROPOSED AD-M^{2}PCC FOR LC-PMSM

To solve the aforementioned issues, an AD-M^{2}PCC scheme is proposed for stabilizing the LC-PMSM system, which is elaborated below.

A. Simplified Reduced-Order Predictive Model

It is noted from the predictive model of typical MPCC in (8) that $\mathbf{A}_d$, $\mathbf{B}_d$, and $\mathbf{D}_d$ contain a time-varying parameter ω_e, which means they must be updated at each T_s online. Moreover, the matrix $\mathbf{A}$ is six order and its exponentiation operations should be performed multiple times, significantly increasing the computational burden. To tackle this problem, a simplified inverter-side current predictive model with a reduced order is established.

Following the power flow in Fig. 2, it can be seen that the inverter-side current is directly controlled by the inverter voltage. Hence, the inverter-side current predictive model can be formulated by the first-order Taylor series expansion, i.e., the forward Euler discretization as

$$\mathbf{i}_{f,k+1} = \mathbf{A}_f \mathbf{i}_{f,k} + \mathbf{B}_f \left(\mathbf{v}_{i,k} - \mathbf{v}_{s,k}\right) \tag{13}$$

where the coefficient matrices $\mathbf{A}_f = \begin{bmatrix} 1 & T_s\omega_{e,k} \\ -T_s\omega_{e,k} & 1 \end{bmatrix}$, and $\mathbf{B}_f = \begin{bmatrix} T_s/L_f & 0 \\ 0 & T_s/L_f \end{bmatrix}$. $\mathbf{i}_{f,k} = [i_{fd,k} \;\; i_{fq,k}]^T$ and $\mathbf{i}_{f,k+1} = [i_{fd,k+1} \;\; i_{fq,k+1}]^T$.

Further, taking delay compensation into account, the simplified predictive model is rewritten as

$$\mathbf{i}_{f,k+2} = \mathbf{A}_f \mathbf{i}_{f,k+1} + \mathbf{B}_f (\mathbf{v}_{i,k+1} - \mathbf{v}_{s,k+1}) \tag{14}$$

where $\mathbf{i}_{f,k+1}$ is obtained by applying the optimal voltage vector at the previous T_s to (13).

Note that $\mathbf{v}_{s,k+1}$ should also be predicted in (14). Still based on the Euler discretization, the $(k+1)$th step filter capacitor voltage is predicted as

$$\mathbf{v}_{s,k+1} = \mathbf{A}_v \mathbf{v}_{s,k} + \mathbf{B}_v (\mathbf{i}_{f,k} - \mathbf{i}_{s,k}) \tag{15}$$

where $\mathbf{A}_v = \begin{bmatrix} 1 & T_s\omega_{e,k} \\ -T_s\omega_{e,k} & 1 \end{bmatrix}$, $\mathbf{B}_v = \begin{bmatrix} T_s/C_f & 0 \\ 0 & T_s/C_f \end{bmatrix}$, $\mathbf{v}_{s,k} = [v_{sd,k} \;\; v_{sq,k}]^T$ and $\mathbf{v}_{s,k+1} = [v_{sd,k+1} \;\; v_{sq,k+1}]^T$.

By comparing (14) with the typical predictive model from (6)–(9), it can be concluded that the proposed simplified predictive model is essentially a reduced-order predictive model, which avoids multiple online exponentiation operations of the sixth-order matrices. Hence, it can significantly reduce the computational burden.

B. Cost Function and Baseline MPCC Design

Normally, the control target of the inner current loop is the stator-current reference tracking. To simplify the control complexity, an inverter-side current reference tracking control is established, which can indirectly realize the vector control of the PMSM. Due to the existence of the filter capacitor branch, the motor-side stator current is not equal to the inverter-side current. Hence, it is necessary to first calculate the inverter-side current reference.

Utilizing the steady-state equilibrium point of the dynamic model in (1), and setting $i_{sd} = i_{sd}^*$, $i_{sq} = i_{sq}^*$, and $\dot{\mathbf{x}} = 0$,

the dq-axis inverter-side current references i_{fd}^* and i_{fq}^* can be derived as

$$\begin{cases} i_{fd}^* = i_{sd}^* - \omega_{e,k} C_f \left(R_s i_{sq}^* + \omega_{e,k} L_s i_{sd}^* + \omega_{e,k} \psi_f \right) \\ i_{fq}^* = i_{sq}^* + \omega_{e,k} C_f \left(R_s i_{sd}^* - \omega_{e,k} L_s i_{sq}^* \right) \end{cases} \tag{16}$$

where i_{sd}^* equals to 0, and i_{sq}^* is calculated from the outer speed control loop.

Then, the cost function for tracking the inverter-side current reference is constructed below

$$\begin{aligned} J &= \left\| \mathbf{i}_f^* - \mathbf{i}_{f,k+2} \right\|^2 \\ &= \left(i_{fd}^* - i_{fd,k+2} \right)^2 + \left(i_{fq}^* - i_{fq,k+2} \right)^2 \end{aligned} \tag{17}$$

where $\mathbf{i}_f^* = [i_{fd}^* \quad i_{fq}^*]^T$ is inverter-side current reference matrix obtained from (16).

From (17), the predictive model $\mathbf{i}_{f,k+2}$ still requires to repeatedly execute to minimize J. To avoid the repeated computation of the predictive model and considering the convenience of AD integration, a baseline MPCC is designed based on voltage-reference tracking. Using the deadbeat principle, it is assumed that the inverter-side current can track its reference over two sampling periods. Thus, setting $\mathbf{i}_f^* = \mathbf{i}_{f,k+2}$ in (17) yields the inverter voltage reference $\mathbf{v}_i^*$ as

$$\mathbf{v}_i^* = \mathbf{B}_f^{-1} \left(\mathbf{i}_f^* - \mathbf{A}_f \mathbf{i}_{f,k+1} \right) + \mathbf{v}_{s,k+1}. \tag{18}$$

Hence, $\mathbf{v}_i^*$ forms the proposed baseline MPCC controller, which can be implemented using different predictive architectures, either finite-set MPCC or modulated ones. In Section IV-D, a modulated MPCC scheme is constructed to obtain good resonance suppression and steady-state performance, which will be elaborated on later.

C. Active-Damping Integration

Note that the baseline MPCC designed in (18) does not consider resonance suppression. To handle the resonance problem of the LC-PMSM system, an AD technique is further integrated into the baseline MPCC, which is implemented by adding a virtual resistor in parallel with the filter capacitor, as explained below.

1) Resonance-Damping Mechanism: The schematic of resonance damping for LC-PMSM using a resistor in parallel with the filter capacitor is depicted in Fig. 5. To facilitate the resonance-damping analysis, the dq-axis is assumed to be decoupled and R_s is neglected since it is very small. Taking the q-axis equivalent circuit as an example, the transfer function from inverter voltage to stator current is derived as

$$\begin{aligned} G_{\text{ad}}(s) &= \frac{i_{sq}(s)}{v_{iq}(s)} \\ &= \frac{1}{C_f L_f L_s s^3 + \underbrace{\left(L_f L_s / R_v \right) s^2}_{\text{damping term}} + \left(L_f + L_s \right) s}. \end{aligned} \tag{19}$$

It can observed from (19) that compared to the original system without a paralleled resistor (i.e., $R_v = \infty$), the inclusion of R_v introduces a damping term (i.e., s^2-related term) to the denominator. Hence, it can provide certain resonance-suppression capability. Moreover, the bode plots of $G_d(s)$ with

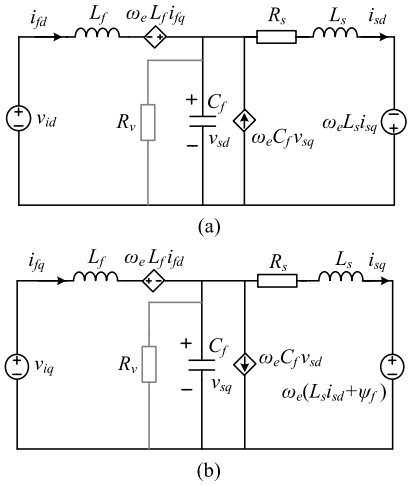

Fig. 5. Schematic of resonance damping for LC-PMSM using a resistor in parallel with C_f. (a) d-axis. (b) q-axis.

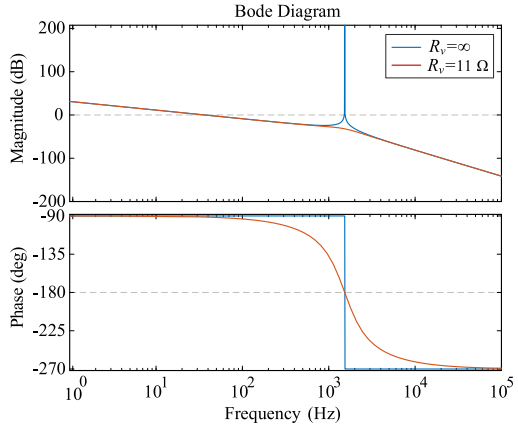

Fig. 6. Bode plots of $G_{\text{ad}}(s)$ with $R_v = 11$ and without damping (i.e., $R_v = \infty$).

$R_v = 11$ and $R_v = \infty$ (i.e., without damping) are compared in Fig. 6 based on the system parameters in Table I. Same conclusions can be drawn that deploying an appropriate R_v in parallel with the filter capacitor can effectively damp the system resonance peak.

2) Active-Damping Embedded Into MPCC: To avoid the power loss of a physical resistor in Fig. 5, a virtual R_v is employed to emulate the damping effect of a real one. The equivalent block diagram of the AD scheme applicable for MPCC in a complex-vector form is shown in Fig. 7. In Fig. 7(a), a virtual resistor R_v is added in parallel with the filter capacitor to provide resonance damping, where m_o is the modulation ratio, T_d is the system delay, and $\mathbf{e}_{dq}$ is the disturbance term related to PMSM's back electromotive force. Through certain equivalent transformations, Fig. 7(b) forms the adopted AD technique for digital implementation. It indicates that by introducing capacitor-current feedback with a damping factor to the baseline MPCC, a virtual resistor R_v in parallel with the filter capacitor C_f can be simulated. Correspondingly, the inverter voltage reference or control input command of AD-based MPCC can be derived by modifying the $\mathbf{v}_i^*$ in (18) as

$$\mathbf{v}_i^* = \mathbf{B}_f^{-1} (\mathbf{i}_f^* - \mathbf{A}_f \mathbf{i}_{f,k+1}) + \mathbf{v}_{s,k+1} - \frac{L_f}{C_f R_v} \mathbf{i}_{c,k} \tag{20}$$

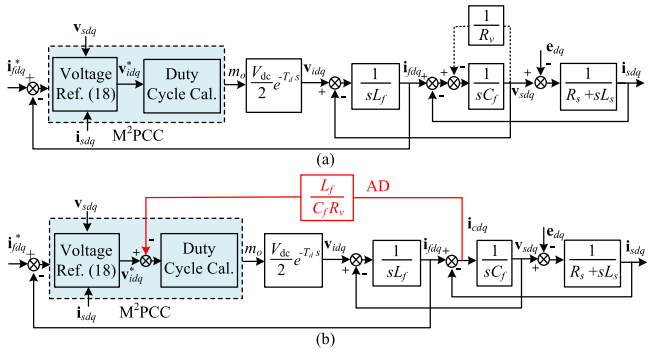

Fig. 7. Complex-vector-form AD scheme for the proposed MPCC. (a) Virtual resistor in parallel with C_f. (b) Equivalent capacitor-current-feedback AD for actual implementation.

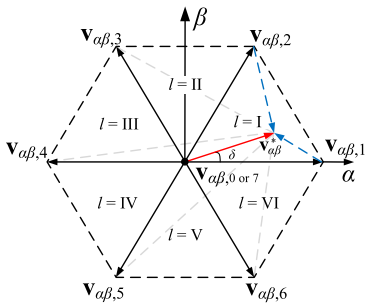

Fig. 8. Diagram of sectors and basic voltage vectors of a VSI.

where the filter capacitor current $\mathbf{i}_{c,k} = \mathbf{i}_{f,k} - \mathbf{i}_{s,k}$, which can either be measured or estimated [12]. $(L_f/C_f R_v)$ is the damping factor with R_v being the virtual resistor to be designed.

Hence, (20) forms the proposed AD-MPCC framework. By properly setting the value of R_v, satisfactory resonance-suppression capability can be achieved. It is worth mentioning that the designed AD term is directly added to the inverter voltage reference, thus it does not hamper the main current control.

D. Low-Complexity AD-M²PCC Design

As is known, the discrete nature of typical MPCC leads to a variable switching frequency, which is not conducive to the filter's design. In contrast, modulated MPCC methods apply multiple voltage vectors during a sampling period, thus possessing the advantages of lower steady-state current ripples and fixed switching frequency. Herein, based on the AD-based MPCC in (20), a low-complexity AD-M²PCC scheme is designed for the LC-PMSM system.

1) Candidate Vector Selection: Fig. 8 shows the diagram of sectors and basic voltage vectors of a VSI. The essence of AD-M²PCC is selecting two active vectors and one zero vector in Table II to optimally track the inverter voltage reference in $\alpha\beta$ reference frame, i.e., $\mathbf{v}^*_{\alpha\beta} = \mathbf{C}^{-1}_{\text{park}}\mathbf{v}^*_i = [v^*_\alpha \quad v^*_\beta]^T$. Therefore, the first problem is to determine which three vectors should be selected as the candidate vectors in each sector. It can be deduced from Fig. 8 that two active vectors adjacent to $\mathbf{v}^*_{\alpha\beta}$ in each sector should be selected as the candidate active vectors since they can achieve minimized reference tracking errors. For example, if $\mathbf{v}^*_{\alpha\beta}$ is located in sector I, the reference tracking error of each vector is determined by the length of the dotted line in Fig. 8. That is to say, $\mathbf{v}_{\alpha\beta,1}$ and $\mathbf{v}_{\alpha\beta,2}$ should be chosen as the two active vectors. Based on this principle, the mapping relationship between the sector l and its candidate active vectors $(\mathbf{v}_{\alpha\beta,m}, \mathbf{v}_{\alpha\beta,n})$ is listed in Table III. Regarding the third zero-voltage vector, it is normally selected based on the switching-transition minimization, which will be discussed later.

TABLE III
CANDIDATE ACTIVE VOLTAGE VECTORS IN EACH SECTOR

Sector l	I	II	III	IV	V	VI
First $\mathbf{v}_{\alpha\beta,m}, m =$	1	3	3	5	5	1
Second $\mathbf{v}_{\alpha\beta,n}, n =$	2	2	4	4	6	6
Position of $\mathbf{v}^*_{\alpha\beta}$, $\delta \in$	$[0, \frac{\pi}{3})$	$[\frac{\pi}{3}, \frac{2\pi}{3})$	$[\frac{2\pi}{3}, \pi)$	$[\pi, \frac{4\pi}{3})$	$[\frac{4\pi}{3}, \frac{5\pi}{3})$	$[\frac{5\pi}{3}, 2\pi)$

2) Optimal Duty Cycle Calculation: The optimal duty cycle determines the action time of each candidate vector to minimize the current tracking error. Note that the cost function in (17) has already defined the inverter-side current tracking error in a squared-quadratic-norm form. However, it requires multiple predictions of $\mathbf{i}_{f,k+2}$ when applying three vectors, somewhat increasing the computational amount. To simplify the implementation complexity, the inverter-side current tracking error is first transformed into the inverter voltage tracking error as follows:

$$\begin{aligned} J_i &= \left\| \mathbf{v}^*_{\alpha\beta} - \mathbf{v}_{\alpha\beta,i} \right\|^2 \\ &= \left(v^*_\alpha - v_{\alpha,i}\right)^2 + \left(v^*_\beta - v_{\beta,i}\right)^2 \end{aligned} \tag{21}$$

where $i \in \{m, n, 0\}$ represents the candidate voltage vectors in Table III.

Then, to facilitate the calculation of the optimal duty cycle for each candidate vector, a weighted voltage-reference tracking-error-based cost function is designed as

$$G_l = \sum_{\substack{i\in\{m,n,0\} \\ \text{in sector } l}} d_i^2 J_i \tag{22}$$

where J_i is obtained by (21), and the sector $l \in 1, \ldots, 6$. d_i represents the duty cycle of each candidate vector, satisfying $0 \le d_i \le 1$ and $\sum_{i\in\{m,n,0\}} d_i = 1$.

Then, the optimal duty cycle d_i for each candidate vector can be derived using the Lagrange multipliers to solve the minimization problem of G_l. To be specific, the equality constraint of the duty cycle is first rewritten as

$$g(d_i) = \sum_{i\in\{m,n,0\}} d_i - 1 = 0. \tag{23}$$

Then, the Lagrangian function can be constructed using G_l and $g(d_i)$ as

$$L(d_i, \lambda) = G_l + \lambda g(d_i) \tag{24}$$

where λ represents the Lagrangian multiplier.

To minimize the Lagrangian function above, the gradients of $L(d_i, \lambda)$ concerning d_i and λ should be calculated, which are expressed as

$$\nabla_{d_i,\lambda} L(d_i, \lambda) = \left(\frac{\partial L}{\partial d_i}, \frac{\partial L}{\partial \lambda}\right) = (2J_i d_i + \lambda, g(d_i)). \quad (25)$$

Setting $\nabla_{d_i,\lambda} L(d_i, \lambda) = 0$ yields optimal duty cycle as

$$d_i = -\frac{\lambda}{2J_i}. \quad (26)$$

Further, substituting (26) into the equality constraint in (23), both λ and the optimal duty cycle d_i can be derived as

$$-\frac{\lambda}{2}\sum_{i\in\{m,n,0\}} J_i^{-1} - 1 = 0 \Rightarrow \lambda = -2\left(\sum_{i\in\{m,n,0\}} J_i^{-1}\right)^{-1} \quad (27)$$

$$d_i = J_i^{-1}\left(\sum_{i\in\{m,n,0\}} J_i^{-1}\right)^{-1}. \quad (28)$$

3) Optimal Sector Determination: Normally, substituting (28) into (22) and enumerating six sectors to evaluate the cost function G_l, the optimal sector l_{op} and duty cycles $d_{0,\text{op}}$, $d_{m,\text{op}}$, and $d_{n,\text{op}}$ can be determined to generate pulses. Nonetheless, it should be mentioned that this process still contains six enumeration computations of G_l. Luckily, it can be deduced from Fig. 8 that the resultant vector of the optimal three vectors should be located closest to the reference voltage vector $\mathbf{v}^*_{\alpha\beta}$. In other words, the optimal sector is exactly the sector where $\mathbf{v}^*_{\alpha\beta}$ is located, which can be directly obtained by the angle position of $\mathbf{v}^*_{\alpha\beta}$ as follows:

$$\delta = \arctan\frac{v^*_\beta}{v^*_\alpha}. \quad (29)$$

Hence, by judging the range of θ based on Table III, the optimal sector l_{op} and the resulting optimal three voltage vectors can be directly identified without G_l evaluation processes, further reducing the implementation complexity.

4) Switching Sequence Generation: Finally, to achieve satisfactory steady-state performance with a fixed switching frequency, a symmetrical seven-segment pulse pattern is adopted to synthesize the optimal three vectors, i.e.,

$$\mathbf{S}_{l_{\text{op}}} = \{\underbrace{\mathbf{v}_{\alpha\beta,0}}_{\frac{d_{0,\text{op}}}{4}}, \underbrace{\mathbf{v}_{\alpha\beta,m}}_{\frac{d_{m,\text{op}}}{2}}, \underbrace{\mathbf{v}_{\alpha\beta,n}}_{\frac{d_{n,\text{op}}}{2}}, \underbrace{\mathbf{v}_{\alpha\beta,7}}_{\frac{d_{0,\text{op}}}{2}}, \underbrace{\mathbf{v}_{\alpha\beta,n}}_{\frac{d_{n,\text{op}}}{2}}, \underbrace{\mathbf{v}_{\alpha\beta,m}}_{\frac{d_{m,\text{op}}}{2}}, \underbrace{\mathbf{v}_{\alpha\beta,0}}_{\frac{d_{0,\text{op}}}{4}}\} \quad (30)$$

where $d_{0,\text{op}}$, $d_{m,\text{op}}$, and $d_{n,\text{op}}$ are the optimal duty cycle obtained from (28). $\mathbf{S}_{l_{\text{op}}}$ represents the resulting optimal switching sequence, which will be applied to VSI.

It is notable from (30) that considering the switching-transition minimization, the zero-voltage vector should be selected as $\mathbf{v}_{\alpha\beta,0}$ at the beginning and end, $\mathbf{v}_{\alpha\beta,7}$ at the center of the switching sequence. Finally, a fixed switching frequency is achieved by this seven-segment switching pattern, which can facilitate the LC-filter design and improve the steady-state performance of the system.

The overall block diagram for the digital implementation of the proposed AD-M^{2}PCC scheme for the LC-PMSM system is depicted in Fig. 9.

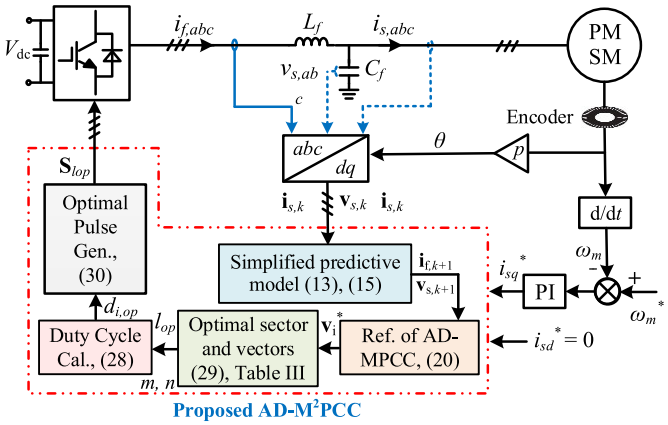

Fig. 9. Block diagram of the proposed AD-M^{2}PCC.

TABLE IV
COMPARISON BETWEEN PROPOSED AD-M^{2}PCC AND TYPICAL MPCC FOR LC-PMSM SYSTEM

Comparison Item	Typical MPCC [27]	Proposed AD-M^{2}PCC
Control objective	3, (i_s, v_s, and i_f)	2, (i_f and AD)
Design parameter	2 weighting factors	1 damping factor
Tuning effort	More	Less
Predictive model	Complex, full order	Simple, reduced order
Computation burden	High	Low
Modulation stage	No	Yes
Switching frequency	Variable	Fixed
Steady-state response	General	Good
Dynamic response	Good	Good
Parameter robustness	General	Good
Explicit AD concept	No, implicit	Yes, intuitive

E. Comparison With Typical MPCC for LC-PMSM

To clearly show the merits of the proposed method for the LC-PMSM system, the comparison between the proposed AD-M^{2}PCC and the state-of-the-art typical MPCC is given in Table IV. Compared with the proposed method, the more control objectives in typical MPCC inevitably introduce two design parameters and a full-order predictive model, which cause a large computational amount and tuning effort. Moreover, typical MPCC is essentially designed based on a finite control set, the lack of modulation stage results in variable switching frequency and moderate steady-state performance compared to the proposed AD-M^{2}PCC. Besides, it is worth mentioning that since the predictive model and AD term of the proposed method do not involve any PMSM parameters, it has stronger robustness and a more intuitive AD concept than those of typical MPCC.

V. PARAMETER DESIGN OF THE LC FILTER AND THE AD-M^{2}PCC CONTROLLER

In this section, the parameter design of the LC filter and the proposed AD-M^{2}PCC controller are elaborated, respectively.

A. Design of the LC Filter

In practice, the maximum switching current ripple of the filter inductor is normally limited within 15%–45% of the rated current [38]. Thus, the filter inductor L_f can be determined according to the maximum peak ripple current ΔI_L as

$$L_f \geq \frac{V_{\rm dc}}{4\sqrt{3}\Delta I_L f_{\rm sw}} \tag{31}$$

where ΔI_L is set to 43% of the rated current in this article.

Based on the nominal parameters of LC-PMSM in Table I, the L_f is calculated as 2 mH. For the selection of the filter capacitor C_f, considering that the capacitor current should be restricted to 5%–15% of the rated active power [38], the constraint condition of C_f is given by

$$C_f \leq \frac{\gamma P_N}{3 \times 2\pi f_0 V_N^2} \tag{32}$$

where γ is the proportion of capacitor current to the rated current, which is set to 15% in this article and the resulting capacitance is 10 μF. P_N and V_N are the rated power and voltage.

Additionally, to effectively filter out the switching harmonics and avoid influencing the fundamental component, the resonant frequency $f_{\rm res}$ generated by the L_f and C_f designed above should be lower than half of the switching frequency and much higher than the fundamental frequency [39], i.e., $f_{\rm res}$ should satisfy the following conditions:

$$10 f_0 \leq f_{\rm res} \leq 0.5 f_{\rm sw}. \tag{33}$$

It is easy to deduce that the designed resonance frequency $f_{\rm res} = 1.53$ kHz, which meets the constraints 667 Hz $\leq f_{\rm res} \leq$ 2.5 kHz.

B. Design of R_v in AD-M^{2}PCC

The proposed AD-M^{2}PCC scheme has only one parameter R_v to be tuned. Since the inverter-side current can be considered as a current source during the steady state, hence, the resonance to be damped occurs only between the filter capacitor C_f and the stator inductor L_s. The s-domain transfer function between the stator current and the inverter-side current can be obtained from Fig. 7 as

$$\frac{\mathbf{i}_{sdq}(s)}{\mathbf{i}_{fdq}(s)} = \frac{\omega_n^2}{s^2 + \frac{1}{R_v C_f} s + \omega_n^2} \tag{34}$$

where the undamped natural frequency $\omega_n = (1/L_s C_f)^{1/2}$, and the virtual resistor R_v can be derived as

$$R_v = \frac{1}{2\xi}\sqrt{\frac{L_s}{C_f}} \tag{35}$$

where ξ denotes the damping ratio, which is set as 0.707 in this article to obtain satisfactory AD and settling time. Hence, the resulting R_v is 11.

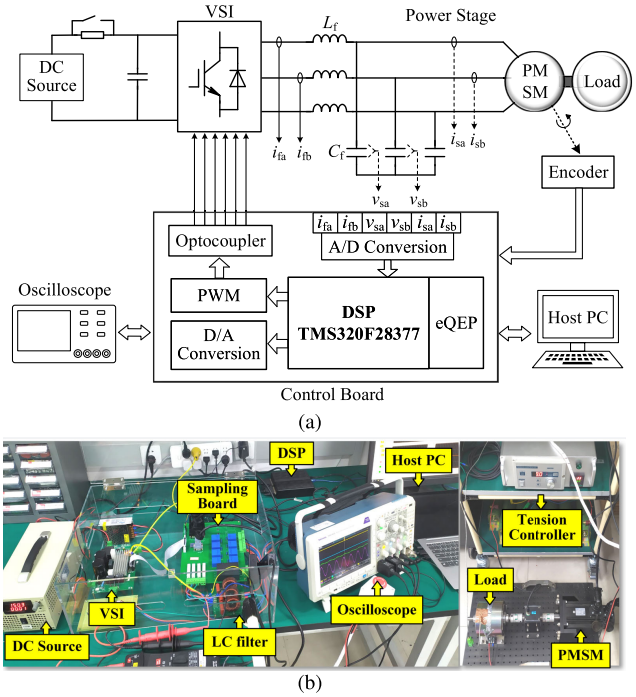

Fig. 10. Experimental setup of an LC-PMSM system for verifying the proposed AD-M^{2}PCC scheme. (a) Configuration diagram. (b) Laboratory platform.

VI. Experimental Verification

A. Testbed Description

It is worth mentioning that few references have reported the modulated MPCC schemes for three-order LC-PMSM due to certain applicability issues. To verify the effectiveness of the proposed control scheme, comparative experiments with typical MPCC in [27], proposed AD-MPCC framework (20) with dual-vector modulation in [31] (i.e., dual-vector AD-MPCC), proposed AD-MPCC framework (20) with three-vector modulation in [35] (i.e., three-vector AD-MPCC), and proposed AD-M^{2}PCC are carried out. Therein, the dual-vector and three-vector AD-MPCC schemes are implemented by modulating the proposed (20) with different duty cycle calculation methods in [31] and [35], respectively.

Moreover, the configuration diagram and the laboratory platform are shown in Fig. 10, which mainly consists of a 2-kW dc source, a three-phase VSI (Mitsubishi DIPIPM PSS20S73F6), an output LC filter, a sampling board (two LEM LV25-P voltage transducers and four LEM LA25-NP current transducers), a surface-mounted PMSM with a 2500-pulses-per-revolution incremental encoder, and a coaxial connected hysteresis-brake load. Meanwhile, the experimental waveforms and data are recorded by an oscilloscope Tektronix MDO3014. The nominal parameters of the LC-PMSM system are listed in Table I. The control algorithms are implemented in the DSP TMS320F28377. For the dual-vector AD-MPCC, three-vector AD-MPCC, and proposed AD-M^{2}PCC, the sampling and switching frequencies are set as 10 and 5 kHz. For a fair comparison, the sampling frequency is set as 25 kHz of the typical MPCC, which aims to obtain a similar average switching frequency of $f_{\rm sw} \approx 5$ kHz [22].

TABLE V
DESIGN PARAMETERS OF FOUR MPCC SCHEMES

Items	Sampling f_s	Switching f_{sw}	Design coefficients
Typical MPCC	25 kHz	$\approx$ 5 kHz	w_v=0.005, w_i=0.001
Dual-vector AD-MPCC	10 kHz	5 kHz	R_v = 11
Three-vector AD-MPCC	10 kHz	5 kHz	R_v = 11
Proposed AD-M^{2}PCC	10 kHz	5 kHz	R_v = 11

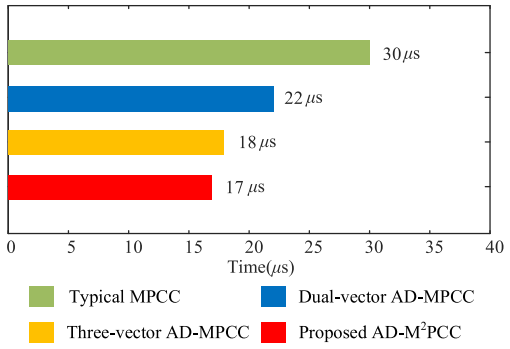

Fig. 11. Execution time comparison of four MPCC methods.

Moreover, all the design parameters of these four MPCC schemes are summarized in Table V.

B. Computational Burden Comparison

To demonstrate the low complexity of the proposed AD-M^{2}PCC, the computational burdens (i.e., execution times) of four MPCC methods are compared in Fig. 11. It can be seen that typical MPCC has the longest execution time among the four MPCC methods due to its most complex predictive model and third-order Taylor series expansion approximation discretization. Since dual-vector and three-vector AD-MPCC are designed based on the proposed simplified predictive model-based MPCC controller in (20), these two methods and the proposed method take similar execution times, which are lower than that of typical MPCC. Besides, dual-vector AD-MPCC has an enumeration process of the cost function, thus leading to a slightly higher computational than that of three-vector AD-MPCC and the proposed method.

C. Resonance-Suppression Performance Comparison

1) Effects of Damping Factor on Resonance Suppression: First, to demonstrate that we have tuned the typical MPCC to be relatively optimal, Fig. 12(a) and (b) shows the experimental results of typical MPCC with different weighting factors w_v and w_i, where $v_{\rm sa}$ and $i_{\rm sa}$ are phase-A capacitor voltage and stator current. It can be seen that either too large or too small of the weighting factors will cause the current oscillations. Based on the criterion in [27] and our experimental observations, setting w_v as 0.005 and w_i as 0.001 in typical MPCC can achieve a satisfactory resonance-suppression performance. Then, to verify the effectiveness of the R_v-design criterion presented in Section V-B, Fig. 12(c) and (d) depicts the experimental results of the resonance-damping performance using the proposed method with different R_v. The results reveal that a larger R_v means underdamping and the resonance cannot be completely suppressed, while a smaller R_v means overdamping, i.e., distorting the fundamental current. Using the predesigned $R_v = 11$ in (35), satisfactory resonance-suppression performance can be obtained. All in all, the designed damping factors above can ensure a fair comparison of these two methods.

TABLE VI
EXPERIMENTAL RESULTS OF STEADY-STATE RESONANCE-DAMPING PERFORMANCE USING FOUR MPCC AT DIFFERENT SPEEDS

Rotor Speed (rpm)	Typical MPCC	Dual-Vector AD-MPCC	Three-Vector AD-MPCC	Proposed AD-M^{2}PCC
	THD of i_{sa}	THD of i_{sa}	THD of i_{sa}	THD of i_{sa}
200	13.62%	8.35%	5.78%	5.46%
400	10.27%	7.83%	4.69%	4.51%
800	11.56%	8.51%	5.28%	4.73%
1000	11.62%	8.89%	5.17%	4.42%

2) Resonance-Suppression Performance Under Different Speeds: The experimental results of resonance-damping performance using four MPCC methods under different speeds during the steady state are evaluated in Figs. 13, 14, and Table VI. Fig. 13 shows the steady-state resonance-suppression performance at 400 r/min. Fig. 14 depicts the corresponding results and harmonic spectra of $i_{\rm sa}$ at 1000 r/min. Table VI illustrates the quantitative comparison results. It can be observed that all four MPCC methods can realize effective resonance suppression at different speeds. Nevertheless, typical MPCC may induce unknown resonant dynamics [see red dotted circle in Fig. 13(a)] due to the single-vector action and unfixed switching frequency, which also cause it to have a widespread harmonic spectrum, the largest ripples, and the highest total harmonic distortion (THD) among four methods. Compared to typical MPCC, the remaining three multivector MPCC can achieve better steady-state performance while ensuring sufficient resonance damping. This is also because these methods are designed based on our proposed control framework in (20). Therein, the three-vector AD-MPCC has similar steady-state performance as the proposed AD-M^{2}PCC due to the similar modulated property, which is better than dual-vector AD-MPCC. Nonetheless, the proposed method still has the lowest THD among the four MPCC methods. Moreover, the stator-current harmonic spectrum of the proposed method is concentrated in the vicinity of the switching frequency and its integer multiples. Hence, it can realize a fixed switching frequency, making it convenient for the design of the *LC* filter compared to typical MPCC.

D. Transient Performance Comparison

Fig. 15 depicts the experimental results of the transient response with speed accelerating from a standstill to 1000 r/min using four MPCC methods. Fig. 16 shows the experimental results of the transient response with a sudden step of load from rated value to 0 using four MPCC methods. The results reveal that the transient performance using

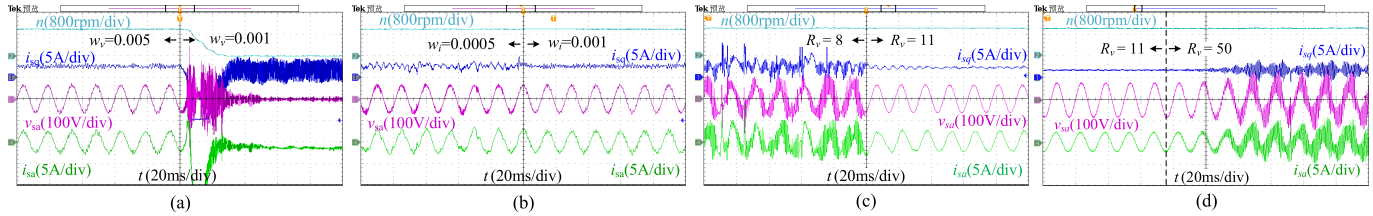

Fig. 12. Resonance-damping performance comparison using typical MPCC and proposed AD-M^{2}PCC under different damping factors. (a) Typical MPCC: $w_v = 0.005 \rightarrow 0.001$, $w_i = 0.001$. (b) Typical MPCC: $w_v = 0.005$, $w_i = 0.0005 \rightarrow 0.001$. (c) AD-M^{2}PCC: $R_v = 8 \rightarrow 11$. (d) AD-M^{2}PCC: $R_v = 11 \rightarrow 50$.

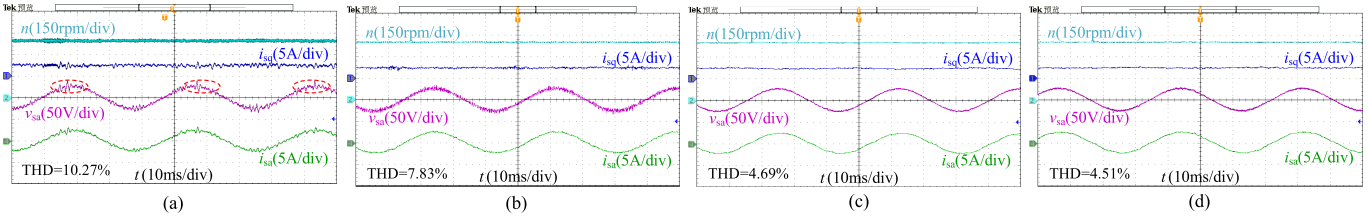

Fig. 13. Resonance-damping performance comparison using four MPCC schemes with $n = 400$ r/min and rated load. (a) Typical MPCC. (b) Dual-vector AD-MPCC. (c) Three-vector AD-MPCC. (d) Proposed AD-M^{2}PCC.

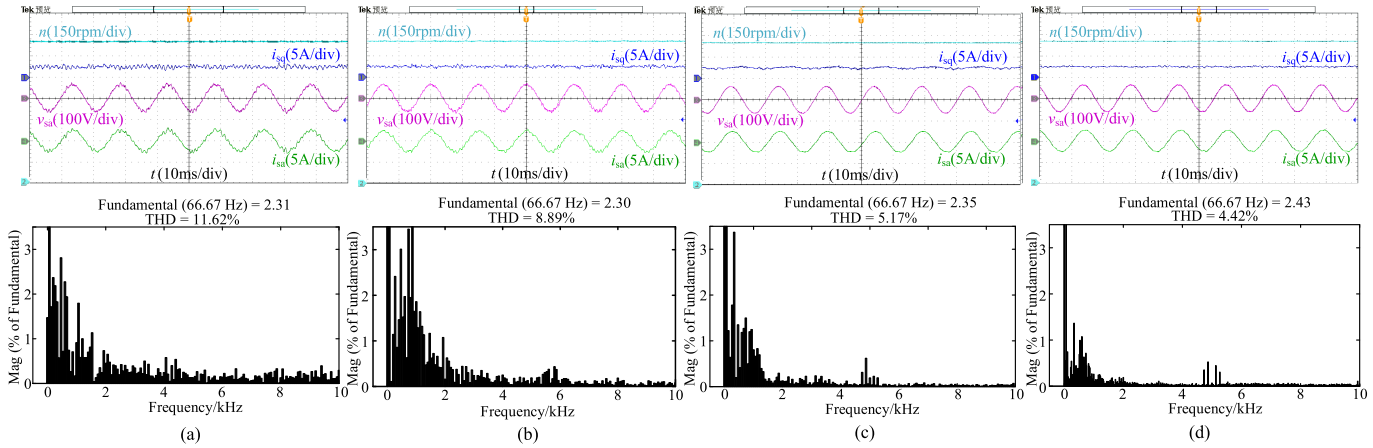

Fig. 14. Resonance-damping performance comparison and harmonic spectra of i_{sa} using four MPCC schemes with $n = 1000$ r/min and rated load. (a) Typical MPCC. (b) Dual-vector AD-MPCC. (c) Three-vector AD-MPCC. (d) Proposed AD-M^{2}PCC.

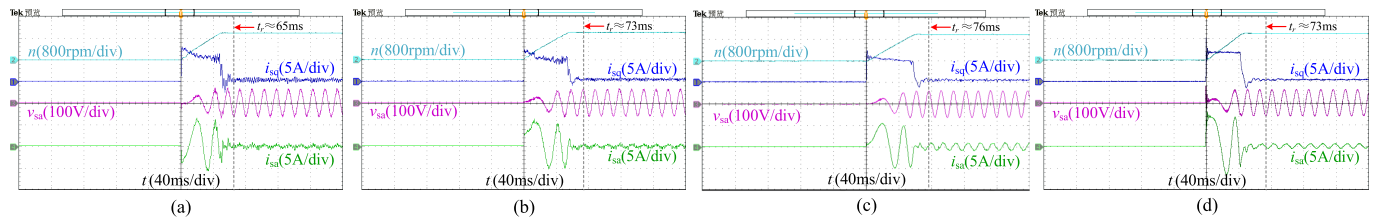

Fig. 15. Transient response comparison using four MPCC schemes with speed accelerating from standstill to 1000 r/min. (a) Typical MPCC. (b) Dual-vector AD-MPCC. (c) Three-vector AD-MPCC. (d) Proposed AD-M^{2}PCC.

four MPCC methods is overall similar. No resonance is excited during the whole transient process and the rotor speed can quickly accelerate to its reference value. It can also be observed that the transient time t_r using typical MPCC is slightly shorter than that of the other MPCC methods. This is because typical MPCC does not include a modulation stage, which has a lower control delay compared to modulated MPCC. Nonetheless, the transient time deviation between the proposed method and the typical MPCC is 8 ms (about 12% slower) while the settling time during the load-step dynamic process is very similar. Hence, the proposed method can achieve a relatively good transient response, which can meet the control requirement practically.

E. Robustness Performance Comparison

To evaluate the robustness to model parameter mismatches, experimental comparisons between typical MPCC and proposed AD-M^{2}PCC under different stator inductor mismatches are shown in Fig. 17, where the mismatches are realized by adjusting the L_s parameter in the controller. Since the dual-vector and three-vector AD-MPCC schemes are designed

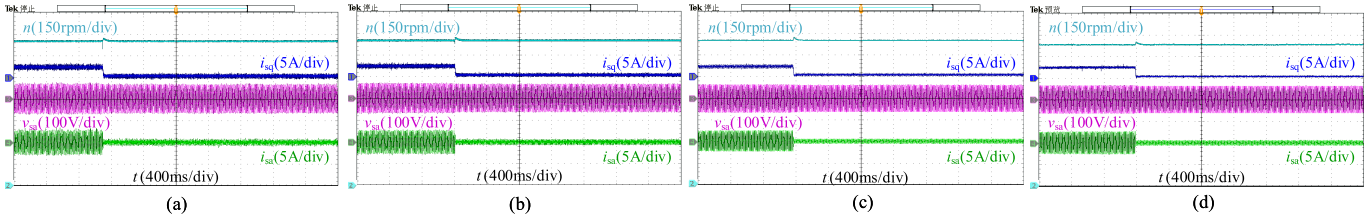

Fig. 16. Transient response comparison using four MPCC schemes with load stepping from rated load to 0. (a) Typical MPCC. (b) Dual-vector AD-MPCC. (c) Three-vector AD-MPCC. (d) Proposed AD-M^{2}PCC.

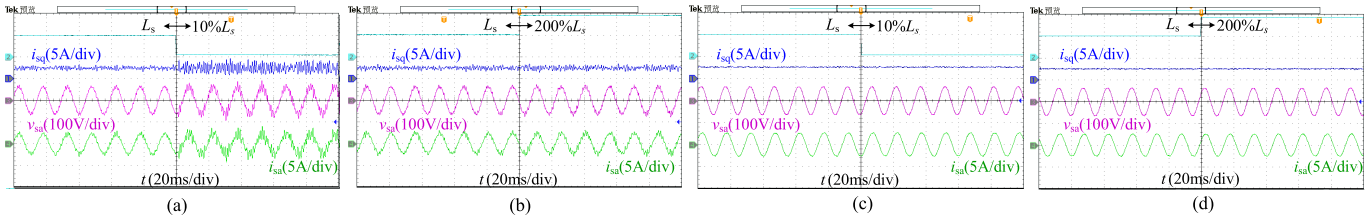

Fig. 17. Robustness performance comparison between typical MPCC and proposed AD-M^{2}PCC under stator-inductor mismatches. (a) Typical MPCC with $10\%L_s$. (b) Typical MPCC with $200\%L_s$. (c) Proposed AD-M^{2}PCC with $10\%L_s$. (d) Proposed AD-M^{2}PCC with $200\%L_s$.

TABLE VII

COMPARISON OF RESONANCE-DAMPING PERFORMANCE USING TYPICAL MPCC AND PROPOSED METHOD WITH *LC*-PARAMETER MISMATCH

Parameter	$70\%L_f$, C_f	$150\%L_f$, C_f	L_f, $70\%C_f$	L_f, $150\%C_f$
Mismatch	THD of i_{sa}	THD of i_{sa}	THD of i_{sa}	THD of i_{sa}
Typical MPCC	12.83%	9.46%	10.67%	11.27%
Proposed method	5.43%	4.12%	4.31%	4.58%

based on the proposed control framework in (20) and the only difference is the modulation fashion, they exhibit the same robustness to L_s mismatches as the proposed AD-M^{2}PCC. As is shown, typical MPCC will cause larger current ripples or even unstable under large L_s mismatches due to the included stator-current predictive model in (12), which will be worse when the stator inductor is underestimated in the controller. In contrast, the proposed method employs a reduced-order predictive model in (20), which does not involve any PMSM parameters. Hence, the L_s mismatches have little effect on the control performance of the proposed method as shown in Fig. 17(c) and (d). In summary, the proposed method has stronger robustness to stator inductor mismatches compared to typical MPCC.

In addition, the quantitative experimental results of the resonance-suppression performance using typical MPCC and the proposed method with *LC*-parameter mismatch are given in Table VII. It can seen that both methods can maintain strong resonance-damping robustness performance under -30% and $+50\%$ mismatches of L_f and C_f. Moreover, both two methods are more sensitive to the underestimation of the real filter inductance in the controller, resulting in a slight increase in the THD. In summary, the proposed AD-M^{2}PCC has stronger robustness to various model mismatches compared to typical MPCC.

F. Comparison to PMSM Drives Without LC Filter

Finally, we compare the dynamic response of q-axis reference current tracking in PMSM without *LC* filter and *LC*-PMSM system based on our proposed M^{2}PCC framework, which is shown in Fig. 18. For PMSM without *LC* filter, the delay-compensated MPCC is designed based on (20), where the AD is removed and the inverter-side current predictive model is replaced with the stator-current predictive model of typical PMSM as follows:

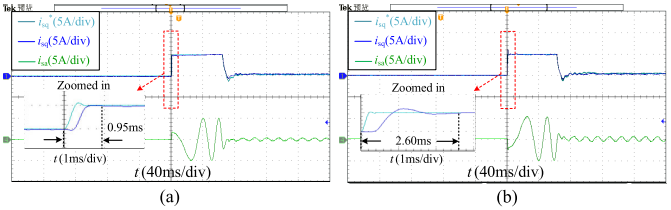

Fig. 18. Performance comparison of q-axis reference current tracking in PMSM without *LC* filter and *LC*-PMSM system using the proposed method. (a) PMSM system w/o *LC* filter. (b) *LC*-PMSM system.

$$\mathbf{v}_i^* = \mathbf{B}_L^{-1}\left(\mathbf{i}_s^* - \mathbf{A}_L\mathbf{i}_{s,k+1} - \mathbf{D}_L\right) \tag{36}$$

where $\mathbf{i}_{s,k+1} = \mathbf{A}_L\mathbf{i}_{s,k} + \mathbf{B}_L\mathbf{v}_{i,k} + \mathbf{D}_L$ and the coefficient matrices are expressed as

$$\mathbf{A}_L = \begin{bmatrix} 1 - T_sR_s/L_s & T_s\omega_{e,k} \\ -T_s\omega_{e,k} & 1 - T_sR_s/L_s \end{bmatrix}$$
$$\mathbf{B}_L = \begin{bmatrix} T_s/L_s & 0 \\ 0 & T_s/L_s \end{bmatrix}, \quad \mathbf{D}_L = \begin{bmatrix} 0 \\ -T_s\omega_{e,k}\psi_f/L_s \end{bmatrix}. \tag{37}$$

In addition, for a fair comparison, the same three-vector modulation technique in (28) and (30) is employed. It can be seen from Fig. 18 that due to the inclusion of the *LC* filter, the stator-current dynamic tracking response of the *LC*-PMSM system is slower than that of PMSM without *LC* filter. These results are consistent with the frequency-domain analysis in Section II-B. Nevertheless, the dynamic tracking time of 2.6 ms of the proposed method is still sufficient to meet the requirements in practical applications.

VII. CONCLUSION

This article presents an AD-M^{2}PCC scheme to stabilize the *LC*-PMSM system. A simplified predictive model and a

baseline MPCC for control of inverter-side current are first constructed, which have reduced computational complexity and enhanced robustness to model mismatches. Then, a capacitor-current-feedback AD technique is integrated into the MPCC, effectively damping the system resonance. Further, a modulated AD-M^{2}PCC scheme is proposed to ensure satisfactory steady-state tracking accuracy and fixed switching frequency. Comparative experimental results validate the superiority of the proposed scheme over typical MPCC.

REFERENCES

[1] X. Li, W. Tian, X. Gao, Q. Yang, and R. Kennel, "A generalized observer-based robust predictive current control strategy for PMSM drive system," *IEEE Trans. Ind. Electron.*, vol. 69, no. 2, pp. 1322–1332, Feb. 2022.

[2] C. Zheng, T. Dragicevic, B. Majmunovic, and F. Blaabjerg, "Constrained modulated model-predictive control of an LC-filtered voltage-source converter," *IEEE Trans. Power Electron.*, vol. 35, no. 2, pp. 1967–1977, Feb. 2020.

[3] S. K. Mazumder et al., "Overview of wide/ultrawide bandgap power semiconductor devices for distributed energy resources," *IEEE J. Emerg. Sel. Topics Power Electron.*, vol. 11, no. 4, pp. 3957–3982, Aug. 2023, doi: 10.1109/JESTPE.2023.3277828.

[4] H. Abu-Rub, S. Bayhan, S. Moinoddin, M. Malinowski, and J. Guzinski, "Medium-voltage drives: Challenges and existing technology," *IEEE Power Electron. Mag.*, vol. 3, no. 2, pp. 29–41, Jun. 2016.

[5] A. K. Morya et al., "Wide bandgap devices in AC electric drives: Opportunities and challenges," *IEEE Trans. Transport. Electrific.*, vol. 5, no. 1, pp. 3–20, Mar. 2019.

[6] Y. Jiang, W. Wu, Y. He, H. S. Chung, and F. Blaabjerg, "New passive filter design method for overvoltage suppression and bearing currents mitigation in a long cable based PWM inverter-fed motor drive system," *IEEE Trans. Power Electron.*, vol. 32, no. 10, pp. 7882–7893, Oct. 2017.

[7] E. Velander et al., "An ultralow loss inductorless dv/dt filter concept for medium-power voltage source motor drive converters with SiC devices," *IEEE Trans. Power Electron.*, vol. 33, no. 7, pp. 6072–6081, Jul. 2018.

[8] P. Mishra and R. Maheshwari, "Design, analysis, and impacts of sinusoidal LC filter on pulsewidth modulated inverter fed-induction motor drive," *IEEE Trans. Ind. Electron.*, vol. 67, no. 4, pp. 2678–2688, Apr. 2020.

[9] S. Baek, Y. Cho, B.-G. Cho, and C. Hong, "Performance comparison between two-level and three-level SiC-based VFD applications with output filters," *IEEE Trans. Ind. Appl.*, vol. 55, no. 5, pp. 4770–4779, Sep. 2019.

[10] J. Salomäki, M. Hinkkanen, and J. Luomi, "Influence of inverter output filter on maximum torque and speed of PMSM drives," *IEEE Trans. Ind. Appl.*, vol. 44, no. 1, pp. 153–160, Jan. 2008.

[11] Z. Lyu and L. Wu, "Current control scheme for LC-equipped PMSM drive considering decoupling and resonance suppression in synchronous complex-vector frame," *IEEE J. Emerg. Sel. Topics Power Electron.*, vol. 11, no. 2, pp. 2061–2073, Apr. 2023.

[12] C. Zheng, T. Dragicevic, and F. Blaabjerg, "Current-sensorless finite-set model predictive control for LC-filtered voltage source inverters," *IEEE Trans. Power Electron.*, vol. 35, no. 1, pp. 1086–1095, Jan. 2020.

[13] R. Pe na-Alzola, M. Liserre, F. Blaabjerg, R. Sebastián, J. Dannehl, and F. W. Fuchs, "Analysis of the passive damping losses in LCL-filter-based grid converters," *IEEE Trans. Power Electron.*, vol. 28, no. 6, pp. 2642–2646, Jun. 2013.

[14] K. Hatua, A. K. Jain, D. Banerjee, and V. T. Ranganathan, "Active damping of output *LC* filter resonance for vector-controlled VSI-fed AC motor drives," *IEEE Trans. Ind. Electron.*, vol. 59, no. 1, pp. 334–342, Jan. 2012.

[15] W. Geng, Z. Zhang, and Q. Li, "Analysis and experimental verification of a conventional inverter with output LC filter to drive ironless stator axial-flux PM motor," *IEEE Trans. Transport. Electrific.*, vol. 7, no. 4, pp. 2600–2610, Dec. 2021.

[16] Y. Yao, Y. Huang, F. Peng, J. Dong, and Z. Zhu, "Dynamic-decoupled active damping control method for improving current transient behavior of LCL-equipped high-speed PMSMs," *IEEE Trans. Power Electron.*, vol. 37, no. 3, pp. 3259–3271, Mar. 2022.

[17] P. Mishra and R. Maheshwari, "A simple feedforward approach to stabilize VSI-fed induction motor with filter in RFOC," *IEEE Trans. Ind. Electron.*, vol. 67, no. 12, pp. 10191–10201, Dec. 2020.

[18] M. Yang et al., "Resonance suppression and EMI reduction of GaN-based motor drive with sine wave filter," *IEEE Trans. Ind. Appl.*, vol. 56, no. 3, pp. 2741–2751, May 2020.

[19] P. Karamanakos and T. Geyer, "Guidelines for the design of finite control set model predictive controllers," *IEEE Trans. Power Electron.*, vol. 35, no. 7, pp. 7434–7450, Jul. 2020.

[20] J. Rodriguez et al., "Latest advances of model predictive control in electrical drives—Part I: Basic concepts and advanced strategies," *IEEE Trans. Power Electron.*, vol. 37, no. 4, pp. 3927–3942, Apr. 2022.

[21] J. Rodriguez et al., "Latest advances of model predictive control in electrical drives—Part II: Applications and benchmarking with classical control methods," *IEEE Trans. Power Electron.*, vol. 37, no. 5, pp. 5047–5061, May 2022.

[22] C. Zheng, Z. Gong, X. Wu, T. Dragicevic, J. Rodriguez, and F. Blaabjerg, "Finite-set quasi-sliding mode predictive control of *LC*-filtered voltage source inverters," *IEEE Trans. Ind. Electron.*, vol. 69, no. 12, pp. 11968–11978, Dec. 2022.

[23] Y. Yang, H. Wen, M. Fan, M. Xie, and R. Chen, "Fast finite-switching-state model predictive control method without weighting factors for T-type three-level three-phase inverters," *IEEE Trans. Ind. Informat.*, vol. 15, no. 3, pp. 1298–1310, Mar. 2019.

[24] L. Guo, N. Jin, C. Gan, L. Xu, and Q. Wang, "An improved model predictive control strategy to reduce common-mode voltage for two-level voltage source inverters considering dead-time effects," *IEEE Trans. Ind. Electron.*, vol. 66, no. 5, pp. 3561–3572, May 2019.

[25] F. Donoso, A. Mora, R. Cárdenas, A. Angulo, D. Sáez, and M. Rivera, "Finite-set model-predictive control strategies for a 3L-NPC inverter operating with fixed switching frequency," *IEEE Trans. Ind. Electron.*, vol. 65, no. 5, pp. 3954–3965, May 2018.

[26] T. Laczynski and A. Mertens, "Predictive stator current control for medium voltage drives with LC filters," *IEEE Trans. Power Electron.*, vol. 24, no. 11, pp. 2427–2435, Nov. 2009.

[27] C. Xue, D. Zhou, and Y. Li, "Finite-control-set model predictive control for three-level NPC inverter-fed PMSM drives with *LC* filter," *IEEE Trans. Ind. Electron.*, vol. 68, no. 12, pp. 11980–11991, Dec. 2021.

[28] T. Geyer, P. Karamanakos, and R. Kennel, "On the benefit of long-horizon direct model predictive control for drives with LC filters," in *Proc. IEEE Energy Convers. Congr. Expo. (ECCE)*, Nov. 2014, pp. 3520–3527.

[29] S. Vazquez, E. Zafra, R. P. Aguilera, T. Geyer, J. I. Leon, and L. G. Franquelo, "Prediction model with harmonic load current components for FCS-MPC of an uninterruptible power supply," *IEEE Trans. Power Electron.*, vol. 37, no. 1, pp. 322–331, Jan. 2022.

[30] Y. Zhang, Y. Bai, and H. Yang, "A universal multiple-vector-based model predictive control of induction motor drives," *IEEE Trans. Power Electron.*, vol. 33, no. 8, pp. 6957–6969, Aug. 2018.

[31] Y. Yang, J. Pan, H. Wen, Z. Zhang, Z. Ke, and L. Xu, "Double-vector model predictive control for single-phase five-level actively clamped converters," *IEEE Trans. Transport. Electrific.*, vol. 5, no. 4, pp. 1202–1213, Dec. 2019.

[32] C. Wang, J. Ji, H. Tang, T. Tao, and W. Zhao, "Improved model predictive current control for linear Vernier permanent-magnet motor with efficient voltage vectors selection," *IEEE Trans. Ind. Electron.*, vol. 70, no. 3, pp. 2833–2842, Mar. 2023.

[33] C. Xiong, H. Xu, T. Guan, and P. Zhou, "A constant switching frequency multiple-vector-based model predictive current control of five-phase PMSM with nonsinusoidal back EMF," *IEEE Trans. Ind. Electron.*, vol. 67, no. 3, pp. 1695–1707, Mar. 2020.

[34] B. Xu, Q. Jiang, W. Ji, and S. Ding, "An improved three-vector-based model predictive current control method for surface-mounted PMSM drives," *IEEE Trans. Transport. Electrific.*, vol. 8, no. 4, pp. 4418–4430, Dec. 2022.

[35] X. Li, Z. Xue, L. Zhang, and W. Hua, "A low-complexity three-vector-based model predictive torque control for SPMSM," *IEEE Trans. Power Electron.*, vol. 36, no. 11, pp. 13002–13012, Nov. 2021.

[36] D. Xiao, K. S. Alam, M. Norambuena, M. F. Rahman, and J. Rodriguez, "Modified modulated model predictive control strategy for a grid-connected converter," *IEEE Trans. Ind. Electron.*, vol. 68, no. 1, pp. 575–585, Jan. 2021.

[37] A. Sarajian et al., "Overmodulation methods for modulated model predictive control and space vector modulation," *IEEE Trans. Power Electron.*, vol. 36, no. 4, pp. 4549–4559, Apr. 2021.

[38] Z. Xin, P. Mattavelli, W. Yao, Y. Yang, F. Blaabjerg, and P. C. Loh, "Mitigation of grid-current distortion for LCL-filtered voltage-source inverter with inverter-current feedback control," *IEEE Trans. Power Electron.*, vol. 33, no. 7, pp. 6248–6261, Jul. 2018.

[39] A. Reznik, M. G. Simoes, A. Al-Durra, and S. M. Muyeen, "LCL filter design and performance analysis for grid-interconnected systems," *IEEE Trans. Ind. Appl.*, vol. 50, no. 2, pp. 1225–1232, Mar./Apr. 2014.

Changming Zheng (Member, IEEE) received the B.Eng. degree in electrical engineering and automation and the Ph.D. degree in control theory and control engineering from China University of Petroleum (East China), Qingdao, China, in 2014 and 2020, respectively.

From 2018 to 2020, he was a Visiting Ph.D. Student with the Department of Energy Technology, Aalborg University, Aalborg, Denmark. He has been a Lecturer with the School of Electrical Engineering, China University of Mining and Technology, Xuzhou, China, since 2021. His main research interests include model-predictive control, renewable energy generation, and PMSM drives.

Dr. Zheng was a recipient of the Best Student Paper Award at the 6th IEEE International Conference on Predictive Control of Electrical Drives and Power Electronics (PRECEDE) in 2021.

Miao Xie received the B.Eng. degree in electrical engineering and automation from Xuzhou University of Technology, Xuzhou, China, in 2019, and the M.S. degree in electrical engineering from China University of Mining and Technology, Xuzhou, in 2022, where he is currently pursuing the Ph.D. degree with the School of Electrical Engineering.

His main research interests include model-predictive control and PMSM drives.

Xuanxuan Dong received the B.S. degree in electrical engineering and automation from the School of Electrical and Power Engineering, Changzhou Institute of Technology, Changzhou, China, in 2022. She is currently pursuing the M.S. degree with the School of Electrical Engineering, China University of Mining and Technology, Xuzhou, China.

Her current research interests include model-predictive control and PMSM drives.

Zheng Gong (Member, IEEE) received the B.Eng. and Ph.D. degrees in electrical engineering from China University of Mining and Technology, Xuzhou, China, in 2012 and 2017, respectively.

From September 2015 to 2016, he was with the Department of Energy Technology, Aalborg University, Aalborg, Denmark, as a joint Ph.D. Student. Since 2017, he has been with China University of Mining and Technology, where he is currently an Associate Professor with the School of Electrical Engineering. His research interests include the advanced topology and control for the high-power converters, motor drives, renewable power generations, and high-voltage dc power transmissions.

Tomislav Dragičević (Senior Member, IEEE) received the M.Sc. and Industrial Ph.D. degrees in electrical engineering from the Faculty of Electrical Engineering, University of Zagreb, Zagreb, Croatia, in 2009 and 2013, respectively.

He is currently a Professor with the Technical University of Denmark, Kongens Lyngby, Denmark, where he leads research in the digitization of power converters. He has authored or coauthored more than 150 IEEE journal articles in these areas.

Dr. Dragičević is currently an Associate Editor of IEEE TRANSACTIONS ON INDUSTRIAL ELECTRONICS and IEEE JOURNAL OF EMERGING AND SELECTED TOPICS IN POWER ELECTRONICS and an Editor of *IEEE Industrial Electronics Magazine*.

Jose Rodriguez (Life Fellow, IEEE) received the Engineering degree in electrical engineering from Universidad Tecnica Federico Santa Maria, Valparaiso, Chile, in 1977, and the Dr.-Ing. degree in electrical engineering from the University of Erlangen, Erlangen, Germany, in 1985.

He has been with the Department of Electronics Engineering, Universidad Tecnica Federico Santa Maria, since 1977, where he was a Full Professor and the President. From 2015 to 2019, he was the President of Universidad Andres Bello in Santiago, Santiago, Chile. Since 2022, he has been the President of Universidad San Sebastian, Santiago. He has coauthored two books, several book chapters, and more than 700 journal articles and conference papers. His research interests include multilevel inverters, new converter topologies, control of power converters, and adjustable-speed drives.

Dr. Rodriguez is a member of the Chilean Academy of Engineering. He was a recipient of a number of best paper awards from journals of the IEEE. He was also a recipient of the National Award of Applied Sciences and Technology from the government of Chile in 2014 and the Eugene Mittelmann Award from the Industrial Electronics Society of the IEEE in 2015. From 2014 to 2021, he was included in the list of Highly Cited Researchers published by Web of Science.